NIPES

Journal of Materials Engineering, Structures and Computation

Journal homepage: www.nipesjournals.org.ng

Modelling and Simulation of Transient Thermal Stress Distribution across AISI 1018 Flat Plates at Variable Welding Temperature Regime

Aniekan Essienubong Ikpe [a]*, Michael Okon Bassey[b]

[a] Department of Mechanical Engineering, Akwa Ibom State Polytechnic, Ikot Osurua, PMB 1200, Nigeria,

[b] Department of Mechatronics Engineering, Akwa Ibom State Polytechnic, Ikot Osurua, PMB 1200, Nigeria.

[*]aniekan.ikpe@akwaibompoly.edu.ng

ARTICLE INFORMATION

Article history:
Received 23 June 2023
Revised 19 July 2023
Accepted 29 July 2023
Available online 29 August 2023

Keywords:
Thermal stress, Welding temperature, Mild steel, Flat plate, Temperature gradient

https://doi.org/10.5281/zenodo.8297860

ABSTRACT

In recent times, failure in structural components has been attributed to a lack of improper understanding of material behaviour under welding temperature, during which thermally induced stresses are trapped (residual stress) within the weldment. This study investigated the effects of variable Tungsten Inert Gas (TIG) welding temperature across AISI 1018 flat plates concerning thermal stress distribution using experimental and Finite Element Method at welding temperatures ranging from 6800-9600^{o}F. Thermally-induced stresses of 4244.373 and 4345.894 MPa were obtained from both FEM and Experimental process at a welding temperature of 680^{o}F while the thermally induced stress values at a higher welding temperature of 9600^{o}F for FEM and experimental process were obtained as 10786.858 and 12124.269 MPa. The study revealed a significant correlation established between the experimentally induced thermal stress distribution and the FEM-induced thermal stress distribution. Moreover, thermally induced stresses were observed to increase as the welding temperature also increased and vice versa. Hence, the FEM approach employed in the study can be adopted as a novel technique for modelling, prediction and control of welding temperature to prevent intense welding heat from translating into detrimental defects due to creep mechanism (thermal loading temperature on material geometry), which may result in untimely failure of component materials in welding-related applications.

1. Introduction

Arc welding is a complex thermal process that involves arc physics, heat and mass transfer as well as phase transformation characterized by microstructural alteration of the welded region, during which thermal residual stresses are induced around the welds. In other words, the weld region is heated to a high-temperature gradient depending on the welding technique, causing thermal expansion and contraction of the metal which may result in thermally induced residual stresses and deformations if heat deposition from the welding temperature is not properly controlled [1, 2].

Recent studies have shown that inordinately high welding temperature and voltage can result in a wider weld bead which would subject the weld to thermal stress cracking, increased undercut,

increased defects by side walls of the fusion zones as well as difficulty in removing slags, while setting the amperage too low may produce narrow and irregular beads which would affect the melting rate (fusion) of the metal plates, while gas flow (flow rate) higher than 20 L/min in AISI 1020 can create a turbulent gas flow which allows the infiltration of air in the weld region, thereby, causing porosity [3].

Similarly, another study showed that welding current has a significant effect on the mechanical properties of the weld metal due to the thermal stress induced by the current flowing via the electrode, which depending on the current increases the heat input [4], thus causing thermal stress in the welded zones.

Additionally, thermally induced residual stresses adversely affect the operating conditions of any part produced by fusion welding processes, such as tungsten inert gas welding, especially thermally induced tensile stress distributions can stimulate the formation and propagation of fatigue cracks over some time.

This is due to the thermal and thermo-elastoplastic changes during the welding process, usually taking into account the nonlinearity caused by the phase transition and phase transition plasticity, the microscopic plastic flow that occurs during the phase transition, changes in material properties and heat transfer coefficients as a function of temperature, and radiation boundary conditions and inclusion of solid phase transition effects [5, 6, 7].

However, the application of heat from the TIG welding arc can also cause thermal stress, which gradually produces tensile stress, yield stress and compressive stress depending on the service conditions of the material. In other words, thermal stresses in the weld are transformed into residual stresses, which can lead to premature failure of the weld material characterized by fatigue acceleration, stress propagation, early crack nucleation, and possible fracture [8]. Thus employing the finite element method (FEM) which is principled on the Goldak model heat source, Owunna et al. [9] performed a temperature- and-time-dependent transient thermal analysis of a 10mm thick AISI 1020 mild steel plate using tungsten inert gas (TIG) welding. The simulation is performed for 20 seconds at a welding speed of 1.5 mm/s with a time step of 2.5 seconds.

At each increasing time step, there was intense heat distribution across the melting zone, phase transformation, and helical transient patterns from the weld known as the heat-affected zone (HAZ). The longer the arc heat at a given melting point, the wider the HAZ, resulting in high thermal and residual stress build-ups that can compromise weld integrity. Li et al. [10] carried out a numerical simulation of the inert metal-to-metal welding process considering the grain heterogeneity of stainless steel (SUS301L-HT). The thermal stress is distributed in a trapezoidal manner over the weld area, and the stress recorded at each end of the weld is relatively small.

In the section that is perpendicular to the weld, the thermal stress has a single peak and the peak is located near the centre of the weld. Grain inhomogeneity causes irregular thermal stress distribution in the weld. Another observation was that the stress distribution of the model with grain inhomogeneity is inhomogeneous compared to the conventional model. In the grain inhomogeneity model, grains with high mechanical properties have high thermal stress values during welding. It was observed that due to grain inhomogeneity, the distribution of thermal stresses in the weld zone was not uniform, resulting in rapidly changing stress patterns on adjacent grain boundaries near the weld zone. Chen et al [11], in their study, employed Focused Ion Beam-Digital Image Correlation (FIB-DIC) micro-ring core technology for stress assessment and a sequentially coupled thermomechanical finite element model for estimating the residual stress state near radial and circular TIG welds. The highest hoop and radial tensile residual stresses are observed near the filler

metal–base metal boundary along with the arc stress compression region at the edge of the base metal portion, which correlates with the thermal history and residual stress self-equilibrium. The highly localized temperature distribution around the weld regions was responsible for significant thermally induced residual stresses [12].

Owunna and Ikpe [13] employed an experimental approach and Finite Element Method (FEM) in evaluating the thermally induced residual stress of AISI 1020 mild steel (low carbon) plates associated with the tungsten inert gas (TIG) welding process. The range of residual stresses measured by welding experiments is 144MPa-402Mpa, while that determined by FEM is in the range of 233-477MPa. The results of the induced stress distribution were obtained from a static study in which the heat change of the arc was used as the stress condition, and temperature increase was observed as the Von Mises stress also increased.

Mishchenko and Scotti [14] proposed a method to quantitatively describe the phenomenon of thermal stress generation in welds with different heat-affected zones (HAZ) and different cooling rates using physical simulation and welding thermal stress diagram (WTSD). The results show that the thermal stress profile is controlled by the contraction and expansion of the phase transition in the confinement of the heated area. Therefore, although the heat transferred from the welding arc thermally reacts in the electrode to form solid metal as it cools, the highest residual stresses may not occur at the slowest cooling rates (due to high heat input) or the fastest cooling rates (due to low heat input), it may not occur in the coarse grain range either. Thermal analysis of the AISI 1020 mild steel plate was performed using SOLIDWORKS 2017 version and ESI Visual-Environment 2016 version [15].
Transient temperature profiles and induced stress fields (Von-mise stress, axial stress and thermal stress) were calculated in three dimensions. During the experiment, the average thermal stress recorded on the steel plate was 38,200 MPa. Using the same experimental parameters in the finite element simulation results in an average Von-mise stress of 37,508 MPa, an average axial stress of 30,732 MPa, and an average thermal stress of 20,101 MPa. The results of the study show that elevated welding temperatures cause these stresses to develop continuously around the weldment. Conversely when Vemanaboina et al. [16] welded two different materials (Inconel 625 and stainless steel 316L) using the GTAW process, the deformation and thermally induced residual stresses were observed to fluctuate with the heat input. The peak value of longitudinal stress and transverse stress was measured with a minimum of 145 MPa and a maximum of 180 MPa, while the peak value of longitudinal stress and transverse stress was measured from 145 MPa to 180 MPa in the welding area.

As a result of the variations in thermal gradients, transverse residual stresses can develop in the fusion zone and HAZ of welds when considering dissimilar welds, while the presence of thermal stresses can result in a non-uniform plastic deformation around the weld region. To minimize this, Yelamsetti and Rajyalakshmi [17] suggested controlled temperature gradients around the weld region with adequate application of heat input rates. The aforementioned studies indicate that induced thermal stress from the TIG welding process may be responsible for high residual stresses and deformation on the fusion zone as well as the heat-affected zone (HAZ) of welded metals, which can result in components' material failure depending on the thermal stress cycle [18]. Therefore, transient thermal stress distribution across AISI 1018 flat plates is investigated in this study through modelling and simulation of the thermal stress distribution profile of the flat plate at variable welding temperature regimes. This can provide the basis for the TIG welding process of AISI 1018 flat plates during the design and manufacture of industrial components.

2. Materıals and Methods

The various materials used in the course of conducting this research work are presented in this section. Moreover, the methods adopted to address thermal stress dıstrıbutıon across AISI 1018 flat plates at different weldıng temperatures as well as the governing equations concerning thermal stresses during TIG welding operation are also reported in this section. These served as the basis upon which the result and discussions presented in this paper were obtained.

2.1. Materıals

Materials used in the welding process included the following: 10mm AISI 1018 mild steel plate, argon welding gas, tungsten inert gas welding machine, tensometer, G-Clamp for camping of specimen, vertical milling machine for milling the angles of the specimen, “K” type thermocouple and welding electrode.

2.2. Methods

AISI 1018 low carbon steel plate of 10 mm thickness was used in the study. Each plate was cut at a dimension of 60x40x10 mm (i.e. length x width x thickness) as illustrated in Figure 1. Emery paper with specification (coarse: P24 grit size with 715 µm and fine: P80 grit size with 201 µm) was employed to smoothen and isolate rust and rough particles from the surface of the specimen before TIG welding was applied on the sample in Figure 1. The next procedure was the cleaning of the surface of the specimen to be welded with industrial solvent (acetone), to effectively remove dirt and other unexpected contaminants on the surface of the specimen. By using a vertical milling machine, the plate (see Figure 1) was chamfered (2mm depth) with 45 degrees around the edges to form a groove (V-groove angle) which was attached to the G-clamp. Similarly, the milling angle was achieved with the help of a Milling machine (vertical type). The welding process was conducted on the plates which were attached to the clamp correctly to eliminate misalignment during the welding operation. TIG welding process was applied on the chamfered section of the plate and filing of the same section using a 2% thoriated tungsten electrode. This was achieved through the use of a Dynasty 210 DX welding machine and 100 % Argon as the torch gas to protect the welding region from contaminants. The AISI 1018 mild steel properties proposed for this study are presented in Table 1 while the V-butt specimen of the AISI 1018 mild steel is shown in Figure 1. The TIG welding specifications employed in the welding process are presented in Table 2.

Table 1: Mechanical Properties of AISI 1018

Properties of AISI 1018		**Chemical Compositions of AISI 1018**	
Yield strength	351.571 N/mm^2	Carbon	0.14-0.20 %
Tensile strength	420.507 N/mm^2	Iron	98.81-99.26 %
Elastic modulus	200000 N/mm^2	Manganese	0.60-0.90 %
Poisson's ratio	0.29	Phosphorous	≤ 0.040 %
Mass density	7900 g/cm^3	Sulphur	≤ 0.050 %
Shear modulus	77000 N/mm^2	Silicon	0.10 %
Thermal expansion coefficient	1.5e-005 /Kelvin	Molybdenum	0.15-0.25 %

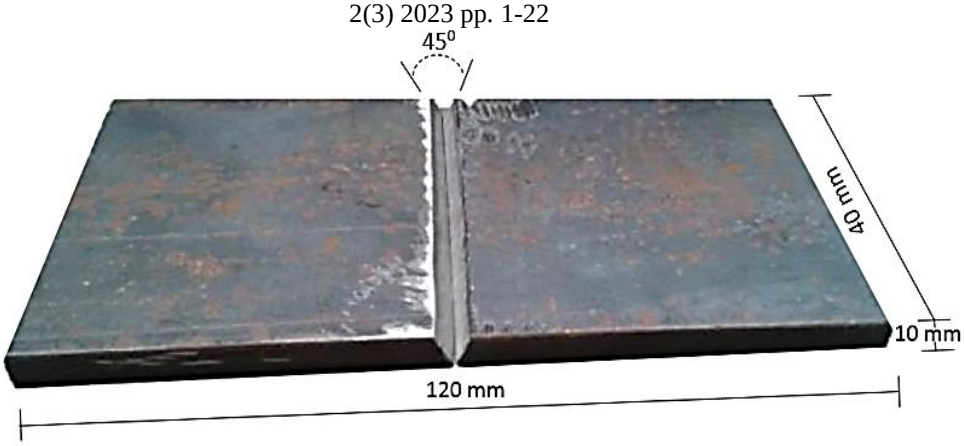

Figure 1. V-butt specimen of mild Steel

Table 2: Materials and specifications used for the welding experimentation

S/N	**Material Specification**	**Welding Specification**
1	Welding Type	Tungsten Inert Gas (TIG)
2	Material	AISI 1018 Low Carbon Steel Plate
3	Material Thickness	10 mm
4	Filler Material	ER 70 S-6
5	Joint Type	Butt Joint (V-groove)
6	Joint Preparation	Abrasive Clean (Sand paper)/Acetone Wipe
7	Joint Gap	2 mm
8	Welding Current	D.C.E.N (Direct Current Electrode Negative)
9	Pulse Width	0.8 Seconds
10	Filler Rod Angle	15^o
11	Welding Torch Angle	45^o
12	Fixed Frequency	60Hz
13	Torch Type	Pro-torch (TIG Torch)
14	Tungsten Type	2% thoriated
15	Tungsten Size	3/1326” Diameter x 25.4 mm
16	Torch Gas	Argon (100%)
17	Heat Input Ratio	10.75 KJ/min
18	Weight of Filler Rod	78.5 Kg/m^2
19	Welding machine	Dynasty 210 DX
20	Clamp type	G-clamp for clamping the work pieces
21	Vertical milling machine	For milling the V-groove angle

Attached to the surface of the workpiece were Type-K thermocouples which allowed the temperature gradient to be recorded at intervals as the arc transverse across the work specimen. In addition, the welding torch was directed through the surface of the plate at a constant speed of 1.72 m/s at a height of 2.5 mm from the workpiece. The welding input parameters were 210-amp current, voltage of 21.00 V, gas flow rate of 19.00 litters/min and welding speed of 3.75 mm/min. These were obtained as optimum values from a Design of Experiment (DOE) for Tungsten Inert Gas (TIG) welding process parameters relative to mechanical properties of AISI 1018 mild steel plate, an extension of the present study previously published by Owunna and Ikpe [19]. The maximum welding temperature varied on each of the Twelve (12) welded samples, which were 6800, 7100, 7350, 7600, 7820, 7960, 8000, 8180, 8400, 8620, 8876 and 9600^oF respectively. The finite Element Method was used for the modelling and simulation of the thermal stress distribution profile of each sample.

2.3. Finite Element Equations for the Welding Process

The variables that were analysed in the course of this study included the stress distribution cycle at variable temperature regimes, in which the governing conditions under welding heat transfer must be satisfied. This can be expressed mathematically in the form of differential equations. In structural mechanic problems, the boundary conditions may be kinematic where the displacements are determined at the end of the simulation or static where the reaction and resultant forces can be seen as the simulation progresses. The specified temperature or heat flow/heat flux or convections may be specified by inputting an initial set of values or process parameters in the computer-aided design tool adopted for thermal analysis. Initial values may be given in the problems where time is involved. In this work, transient thermal analysis is considered for determining the temperatures and other thermal quantities for time-varying thermal loads. The boundary condition of the arc welding temperature field can be determined using the following relationship in Equation 1 [20, 21]:

$$-k\frac{\partial T}{\partial z}| \tag{1}$$

The welding process is considered non-linear due to the temperature distribution across the material surface. Considering a function U(x,y,z,t) of three spatial variables (x,y,z) and the time variable t, the mathematical formulation of the heat equation for the welding condition [22] is given by Equation 2:

$$\frac{\partial u}{\partial t} - \alpha\left(\frac{\partial^2 u}{\partial x^2} + \frac{\partial^2 u}{\partial y^2} + \frac{\partial^2 u}{\partial z^2}\right) = 0 \tag{2}$$

In the physical condition of temperature variation, U(x,y,z,t) denotes the temperature while α denotes the thermal diffusivity. According to Fourier's law, the rate at which thermal energy per unit area during the welding process flows through the surface of the workpiece is proportional to the negative temperature gradient on its surface, which is determined by Equation 3:

$$q = -k\nabla u \tag{3}$$

Thus, *k* and *u* denote the thermal conductivity and temperature. In the absence of work done, the change in internal energy per unit volume of the material (ΔQ) is proportional to the change in temperature (Δu) given by Equation 4:

$$\Delta Q = c_p \rho \Delta u \tag{4}$$

Where *cp* is the specific heat capacity and ρ is the mass density of the material. Selecting zero energy at absolute zero temperature, can be expressed by Equation 5:

$$Q = c_p \rho u \tag{5}$$

When work is done in terms of welding operation and heat sources are present, the expression is given by Equation 6 [23]:

$$c_p \rho \int_{x-\Delta x}^{x+\Delta x}[u(\xi, t+\Delta t) - u(\xi, t-\Delta t)]\, d\xi = c_p \rho \int_{t-\Delta t}^{t+\Delta t}\int_{x-\Delta x}^{x+\Delta x}\frac{\partial u}{\partial \tau} d\xi d\tau \tag{6}$$

When no work is done and there are no heat sources present, the change in internal energy in the interval (x−Δx, x+Δx) is accounted for by the flux of heat across the boundaries. Considering Fourier's law, this is given by Equation 7,

$$k\int_{t-\Delta t}^{t+\Delta t}\left[\frac{\partial u}{\partial x}(x+\Delta x, \tau) - \frac{\partial u}{\partial x}(x-\Delta x, \tau)\right] d\tau = k\int_{t-\Delta t}^{t+\Delta t}\int_{x-\Delta x}^{x+\Delta x}\frac{\partial^2 u}{\partial \xi^2} d\xi dr \tag{7}$$

However, increase in the internal energy in a small spatial region of the workpiece during welding operation is given by Equation 8;

$$x - \Delta x \leq \xi \leq x + \Delta x \tag{8}$$

Increase in the internal energy overtime of welding operation is given by Equation 9:

$$t - \Delta t \leq \tau \leq t + \Delta t \tag{9}$$

Temperature-induced stresses can vary due to several factors depending on the welding sequence, dimensions of the workpiece to be welded, the heat input, mechanical properties of the materials to be welded together, the number of passes of the welding process, and the temperature preheating. After welding operation, the study of weldments is very significant for the prediction of induced stresses due to temperature and examining the dangers of nucleation and fatigue crack propagation. However, stresses and strains induced on the material by welding temperature can cause an increase in the net stress values within the weldment, fatigue crack propagation spread of intergranular cracks as a result of stresses induced by high welding temperature. During the welding operation, temperature distribution along the welding specimen may result in expansion or contraction. Therefore, the thermal strain is given by Equation 10 [24, 25]

$$:\varepsilon_{th} = \alpha \Delta T \tag{10}$$

Where, $\varepsilon_{\mathrm{th}}$ signifies the thermal strain, α signifies the coefficient of thermal expansion and ΔT is the temperature variation. The heating effect determined by Hooke's law is given by the relation in Equation 11 [26]:

$$\begin{bmatrix} \varepsilon_{xx} \\ \varepsilon_{yy} \\ \varepsilon_{zz} \\ \Upsilon_{xy} \\ \Upsilon_{xz} \\ \Upsilon_{yz} \end{bmatrix} = \frac{1}{\mathrm{E}} \begin{bmatrix} 1 & -\mathrm{v} & -\mathrm{v} & 0 & 0 & 0 \\ -\mathrm{v} & 1 & -\mathrm{v} & 0 & 0 & 0 \\ -\mathrm{v} & -\mathrm{v} & 1 & 0 & 0 & 0 \\ 0 & 0 & 0 & (1+\mathrm{v}) & 0 & 0 \\ 0 & 0 & 0 & 0 & (1+\mathrm{v}) & 0 \\ 0 & 0 & 0 & 0 & 0 & (1+\mathrm{v}) \end{bmatrix} \begin{bmatrix} \sigma_{xx} \\ \sigma_{yy} \\ \sigma_{zz} \\ \sigma_{xy} \\ \sigma_{xz} \\ \sigma_{yz} \end{bmatrix} + \alpha \Delta \mathrm{T} \begin{bmatrix} 1 \\ 1 \\ 1 \\ 0 \\ 0 \\ 0 \end{bmatrix} \tag{11}$$

Equation 11 can further be expressed inversely as written in Equation 12:

$$\begin{bmatrix} \sigma_{xx} \\ \sigma_{yy} \\ \sigma_{zz} \\ \sigma_{xy} \\ \sigma_{xz} \\ \sigma_{yz} \end{bmatrix} = \overline{\overline{\mathrm{K}}} \begin{bmatrix} \varepsilon_{xx} \\ \varepsilon_{yy} \\ \varepsilon_{zz} \\ 2\varepsilon_{xy} \\ 2\varepsilon_{xz} \\ 2\varepsilon_{yz} \end{bmatrix} - \frac{\mathrm{E}\alpha\Delta\mathrm{T}}{1-2\mathrm{v}} \begin{bmatrix} 1 \\ 1 \\ 1 \\ 0 \\ 0 \\ 0 \end{bmatrix} \tag{12}$$

The governing partial differential equation for the transient heat conduction is given by Equation 13:

$$K(T)\,(\partial^2 T/\partial x^2) + (\partial^2 T/\partial y^2) + (\partial^2 T/\partial z^2) + Q = \rho(T)\, C_P(T)\,)\, \partial T/\partial t \tag{13}$$

Where, *x*, *y*, *z* represents the Cartesian coordinates, *Q* is the internal heat generated, ρ is the density, *k* is the thermal conductivity, and C_P is the specific heat, are functions of the welding temperature (*T*). Given by Equation 14 Johnson-Mehl-Avrami law can be considered for simulation of phase transformations involving diffusion for welding of steels (austenitic, ferritic-pearlitic and bainitic transformations) under isothermal conditions [27, 28]:

$$p(T,t) = p(T)\left(1 - exp(-(t/\tau_R(T))^{n(T)}\right) \quad (14)$$

Where, p is the phase proportion derived after an infinite time at temperature T, τ_R is the delay time and n is the exponent related to the reaction speed between the arc electrode and the workpiece during welding operation. Considering the martensitic transformations, Koistinen-Marburger law can best describe the relationship given by Equation 15 [29]:

$$p_m(T) = p_m\left(1 - exp\left(-b(M_s - T)\right)\right) \qquad with\ T \leq M_s \quad (15)$$

Where p_m is the phase proportion derived at an infinitely low temperature, M_s and b characterise initial transformation temperature. The parameters proposed by Johnson-Mehl-Avrami model was extracted from the Continuous Cooling Transformation (CCT) diagram, based on the cooling speed, inserted in the finite element analysis. The martensite fraction as a function of temperature at each point of martensite transformation is given by Equation 16:

$$m = 1 - exp\{-K\{M_s - T\}\} \quad (16)$$

Where, m represents the martensite fraction, M_s is the initial temperature for the martensite transformation, k is a constant and T is the temperature. Given by the relation in Equation 17, dilatation applied during martensite transformation is expressed in Equation 18 [30, 31]:

$$\alpha = \Delta m\ f\ \varepsilon^{tr} \quad (17)$$

Where α represents the total strain across the martensite transformation range, Δm is the increase in martensite fraction as a function of temperature, f is the martensite fraction as a function of cooling rate, and is ε^{tr} the transformation strain. Given by Equation 18, the heat loss by free convection is based on Newton's law, where the coefficient of convective heat transfer is assumed to vary with both temperature and orientation of the boundary [32, 33]:

$$q_c = (k\ Nu/L)(T - T_a) \quad (18)$$

Where, k represents the thermal conductivity of the material, L is the characteristic length of the mild steel plate, T_a is the ambient temperature and Nu is the Nusselt number given by Equation 19:

$$Nu = 5.67\ Pr^{1/3}\ Gr^{1/3} \quad (19)$$

Where Pr represents the Prandtl number and Gr is the Grashof number, both being functions of ambient air properties and temperature differences between the weldment the environment. Heat loss as a result of radiation may be significant when temperature difference between the weldments and environment is high. This is given by the relation proposed by standard Stefan-Boltzman in Equation 20: Heat loss due to radiation can be significant if the temperature difference between the weld and the environment is large. This is given by the standard Stefan-Boltzmann relation in Equation 20 [34]:

$$q_r = \varepsilon\ \sigma\ (T^4 - T_\alpha{}^4) \quad (20)$$

Where, ε represents the heat emissivity and σ is the Stephan-Boltzman constant. However, the relationships between stress and elastic strain by Hooke's law is given by Equation 21 [35, 36]:

$$\begin{vmatrix} \varepsilon_x' = \frac{1}{E}\left(\sigma_x - v\sigma_y\right), \\ \varepsilon_y' = \frac{1}{E}\left(\sigma_y - v\sigma_y\right), \\ \gamma_{xy}{}' = \frac{1}{G}\,\tau_{xy} \end{vmatrix} \quad (21)$$

The overall stress obtained during TIG welding process must satisfy the following equilibrium conditions (see Equations 22a-b) for the material to exhibit high resistance against the effects of temperature induced stresses on the material [37, 38]:

$$\frac{\partial \sigma_x}{\partial x} + \frac{\partial \tau_{xy}}{\partial y} = 0, \quad (22a)$$

And

$$\frac{\partial \tau_{xy}}{\partial x} + \frac{\partial \sigma_y}{\partial y} = 0. \quad (22b)$$

The total amount of strain in the material after TIG welding must satisfy the following compatibility conditions given in Equation 23:

$$\left[\frac{\partial^2 \varepsilon_x'}{\partial y^2} + \frac{\partial^2 \varepsilon_y'}{\partial x^2} - \frac{\partial^2 \gamma_{xy}'}{\partial x\,\partial y}\right] + \left[\frac{\partial^2 \varepsilon_x''}{\partial y^2} + \frac{\partial^2 \varepsilon_y''}{\partial x^2} - \frac{\partial^2 \gamma_{xy}''}{\partial x\,\partial y}\right] = 0 \quad (23)$$

If the total deformation of the material after TIG welding operation does not meet the compatibility conditions expressed in Equation 23, it is called the incompatibility term (*R*) and can be determined from the plastic deformation. If the value of *R* is not zero, residual stresses may occur in the weld. In this case, R is obtained by Equation 24:

$$R = -\left[\frac{\partial^2 \varepsilon_x''}{\partial y^2} + \frac{\partial^2 \varepsilon_y''}{\partial x^2} - \frac{\partial^2 \gamma_{xy}''}{\partial x \partial y}\right] \quad (24)$$

In the molten pool region of an arc welding, continuity equation for the incompressible fluid is given by Equation 25 [39, 40]:

$$\frac{1}{x}\frac{\partial(x\rho v)}{\partial x} + \frac{\partial(\rho u)}{\partial z} = 0 \quad (25)$$

Where, ρ is density of the fluid, v and u are the axial and radial velocity.

Considering the axial momentum conservation equation, the molten metal in the weld pool and movement of argon shielding gas agrees with Equations 26 and 27 [41]:

$$\rho v\frac{\partial u}{\partial x} + \rho u\frac{\partial u}{\partial z} = -\frac{\partial P}{\partial z} + 2\frac{\partial}{\partial z}\left(\mu\frac{\partial u}{\partial z}\right) + \frac{1}{x}\frac{\partial}{\partial r}\left(x\mu\frac{\partial u}{\partial x}\right) + \frac{1}{x}\frac{\partial}{\partial r}\left(x\mu\frac{\partial v}{\partial z}\right) + j_x B_\theta + \rho g \quad (26)$$

From Equation 26, the radial momentum conservation equation is given by the mathematical relationships in Equation 27;

$$\rho v\frac{\partial v}{\partial x} + \rho u\frac{\partial u}{\partial z} = -\frac{\partial P}{\partial x} + \mu\left(2\frac{1}{x}\frac{\partial}{\partial x}\left(x\frac{\partial v}{\partial x}\right) + \frac{\partial}{\partial z}\left(\frac{\partial v}{\partial z} + \frac{\partial u}{\partial z}\right) - 2\frac{v}{x^2} - j_z B_\theta\right. \quad (27)$$

Where, *P* denotes the pressure and μ is the velocity flow of argon shielding gas used for the welding operation. Solid model of the low carbon steel plate is shown in Figure 2a-b while meshed model is presented in Figure 2c. However, mesh control was applied to the heat source, while curvature based mesh was used due to the ellipsoidal shape of the heat source. The information employed in the simulation process is presented in Table 3. Conversely, the mesh control is applied to the heat

source, and a curvature-based mesh is used due to the elliptical shape of the heat source. The information used during the simulation is shown in Table 3

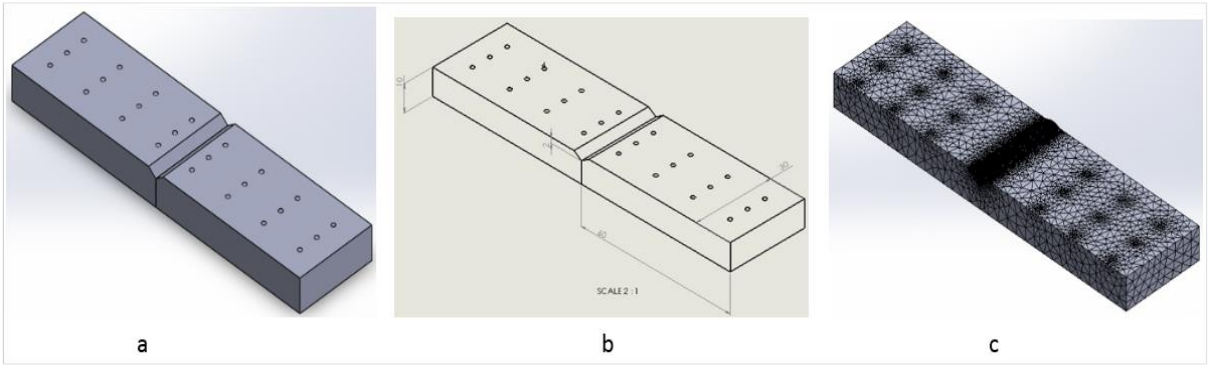

Figure 2. AISI 1018 model of low carbon steel plate

Table 3: Information employed in the simulation process

Model Information for 10 mm Flat Plate	
Study name: TIG weldıng	Mesher Used: Curvature based mesh
Analysis type: Thermal (Transient)	Jacobian points: 4 Points
Mesh type: Solid Mesh	Maximum element size: 3.4556 mm
Solver type: FFEPlus	Minimum element size: 0.69112 mm
Solution type: Transient	Total Nodes: 218728
Total time: 20 Seconds	Total Elements: 154350

3. Results and Dıscussion

To effectively outline the multiplex development which emanates from Tungsten Inert Gas (TIG) welding operation, the entirety of the 3D model of the AISI 1018 steel plate of Low Carbon was deployed.

Thus, deploying Solid Works Finite Element Solver (FES) with transient cum nonlinear thermal solution, which will be precipitated on the convention of heat conduction radiative boundary conditions and convection was achieved at the beginning stage of the simulation operation which produced the prerequisite nodal thermal record.

Similarly, adopting a curvature-typed screen as the lacework and the FFEPlus as the solver in the thermal solution, the separation of the metallic flat plate (workpiece) with screen refinement by the side of the welded zone which will facilitate the proper prediction of the temperature and its residual stress distribution which is corresponding to the steel plate across its section. Additionally, it could be observed that temperature profiles were used as thermal loads in ascertaining the dependent analysis to achieve the residual stress zones.

The application of FEM on thermal analysis remains a viable platform which the residual stress criterion in the steel plate specimen. Practically, the welding process operates in a thermal cycle which originates from heat transfer from the welded region (Heat Affected Zone-HAZ) accompanied by the heat which radiates in the weldment and the entire welded plate. More so, considering a time space of 2.5 seconds for each welding stage was executed, it was observed that the stress spread had more concentration around the weldment and the contours.

Conversely, another discovery was the highest residual von-mises stress point which occurred at each stress profile around the corners and sharp edges which separates the vertical planes and the horizontal planes of the flat plate. (as seen in Figures 3-14), where the flat plates (the two specimens) are conjoined together by TIG welding operation. Additionally, the stress profiles indicate that the von-misses' residual stresses increase to increase temperature. This is clearly shown in the plots of temperature (^{o}F) to the maximum residual stress as shown in Figures 15a-i.

In this study, the TIG welding process includes the control deposition of molten metal involving two cold metal plates. After each welding process (done in sequence), it can be deduced that the welded joint upon cooling resulted in the weld metal being contracted. The effect is the increase in thermal stresses around the weldment which occurred at the gradual reduction of temperature. On the other hand, at a sufficient yield stress value (yield point) there is a deformation of the metal which happens plastically because of the creep mechanism.

Similarly, if we consider the effect of creep mechanism which is the thermal loading temperature on the weld geometry, microstructural phase, properties and characteristics of the material; the thermally induced stresses mentioned previously are confined around the weld region as stress (residual) which can contribute to fracture (brittle property). This can also cause crack propagation or stress corrosion cracking which may lead to failure around the fusion zone during its service life. The situation may occur because the steel plate has some external forces acting upon them (compressive and tensile forces) under welding operation with the corresponding residual stress trapped with the material, hence with an increasing duty cycle which tends to surpass the endurance limit of the material, propagation, causing stress nucleation, cracks and eventual exposure to early failure. The results of thermal stress distribution were created from a static study where the thermal results were used as the loading conditions. The ends of the flat plate and its base were constrained to prevent the effect of displacement, and twenty (20) different weld passes were made using the temperature effect from the thermal study. For an adequate view of the thermally induced residual stress distribution, only one-half of the flat plate was extracted from the simulation since the stresses were distributed uniformly across the two plates as represented in Figures 3-14.

In other words, the Figures illustrate the thermal stress distribution profile at welding temperatures ranging from 6800-9600^{o}F. Each of the figures has a legend characterized by different colours, which has significance to the behaviour of the material when exposed to the welding heat. From the order in which the colours appear on the legend, it can be observed that red colours appear at the top while royal blue colours appear at the bottom. Thermal stress value is attached to red colours, royal blue colours and every other colour on the legend. Thermal stress values attached to the red colour signify the maximum thermal stress distribution resulting from maximum welding temperature while thermal stress values attached to the royal blue colour signify minimum thermal stress distribution resulting from welding temperature. However, thermal stress values attached to orange, lemon, green and sky-blue colours have their severity following red colour. As observed in Figure 3, the maximum thermal stress (von Mises-MPa) value of 4244.373 MPa represented by red colour is produced at a maximum welding temperature of 6800^{o}F. Moreover, the maximum thermal stress (von Mises-MPa) value of 4297.381 MPa represented by red colour is produced at a maximum welding temperature of 7100^{o}F as presented in Figure 4.

Fast-forward to the highest welding temperature employed in this study, maximum thermal stress (von Mises-MPa) value of 10786.858 MPa represented by red colour is produced by a maximum welding temperature of 9600^{o}F. From the trend observed, it is obvious that thermal stress distribution increased proportionately with welding temperature. In other words, an increase in welding temperature results in an increase in thermal stress distribution along the fusion zone of the weldment as shown in Figure 14. This may not be the case in the Heat Affected Zone (HAZ), as the

welding heat reduces due to heat transfer. This correlates with the findings of Mishchenko and Scotti [14], as it was observed that thermal stress distribution progressively decreases along the HAZ. It is obvious with the differences in thermal gradients, the transverse residual stresses are synthesised within the HAZ of the welded joints and the weld. Similarly, this situation can be reduced by modulating the temperature gradients around the weld area with adequate heat requirements at intervals [42]. Also, selection of adequate welding parameters can go a long way in the reduction of residual stress (by 20 to 40 MPa) resulting from thermal gradient during the welding sequence [43]. It can also be recalled that thermal stress operates with the principles of maximum distortion energy criterion which is also known as Von-mises Yield criterion. This forms the component of the Theory of plasticity of ductile materials which indicates that the yielding process in a material begins at second deviatoric stress invariant and when it attains a critical value at that instance. Thus, two important methods are usually deployed in order to minimize the residual induced stress which exist in the fusion zone. These methods are thermal and mechanical Post-Weld treatment- PWT [44, 45]. The main purpose of stress relieving the welded piece (welded material) can be enumerated thus;

1. To acquire dimensional stability which will enhance tolerance in the course of machining operation
2. To synthesis adequate metallurgical structures needed to attain optimum mechanical characteristics.
3. To reduce the risk of exposure of welded workpiece (welded metal) to brittle fracture and stress corrosion during service condition.

In the case of post weld thermal heat treatment for low carbon steels, the metal involved would be subjected to temperature between 1100-1350^{o}F where yield strength of material is reduced to the same level or below the residual stress, hence, minimizing induced stress which occur in the metal. Hatamleh et al. [46] opined that, post weld treatment (mechanical), vibratory method or shot peening approach can be employed for the mitigation of induced stresses. Short Peening method is a cold-working approach that a projected shot is employed upon the circumference of the metal balls and on the outer surface of the weldment, which indentation (small quantity) are impressed upon the face of the fusion zone in order to produce the compressive stress effect.

Certainly, thermal stress that is resident at the top of the weldment must be able to “dominate” for the fatigue crack initiation to happen. On the other hand, compressive stress which emanates from the shot peening reaction will act with respect to tensile residual stresses, depth of compressive stresses, maximum compressive stress, and velocity of shots should be adequately guided, as deep shot impact may have an adverse effect on the induced stress that may bring disastrous outcome. In the same vein, using Vibratory method will involve the use

mechanical vibrating machine to the fusion zone, where the vibrations’ resonance frequency can be controlled, thus integrating the induced stress distribution along with the weldment through plastic deformation of the material grain sizes which will invariably impact sharp stress peaks in structural lattice of the weld region.

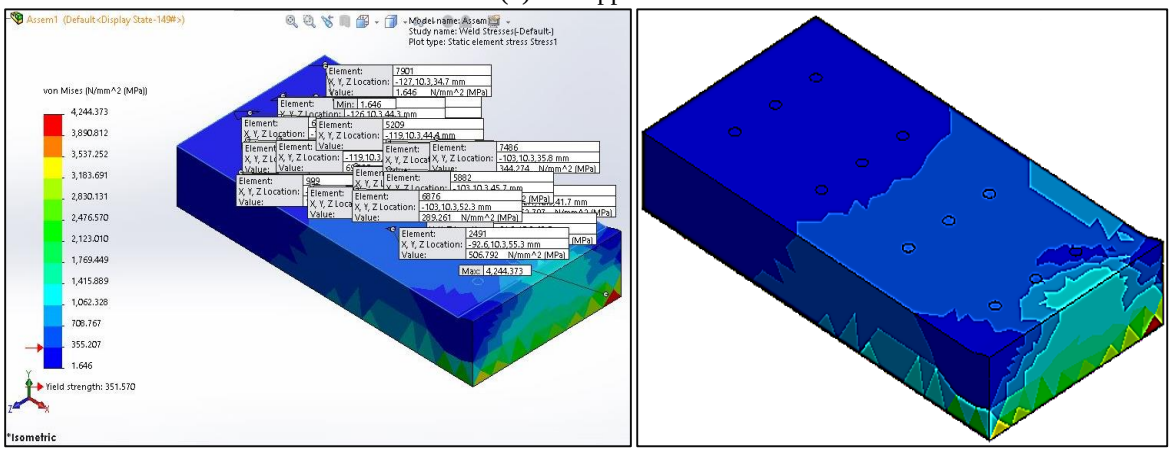

Figure 3. Thermal stress distribution profile at welding temperature of 6800ºF

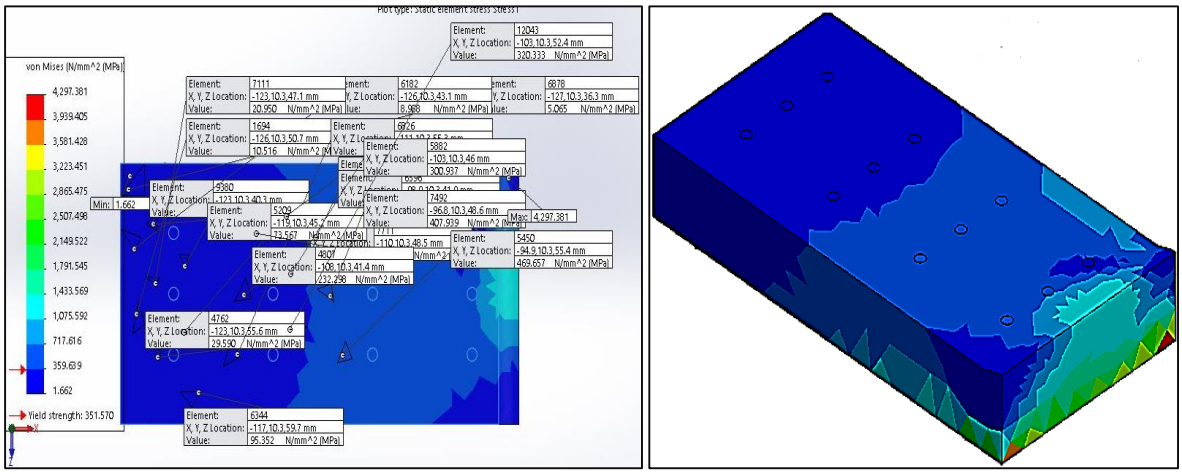

Figure 4. Thermal stress distribution profile at welding temperature of 7100ºF

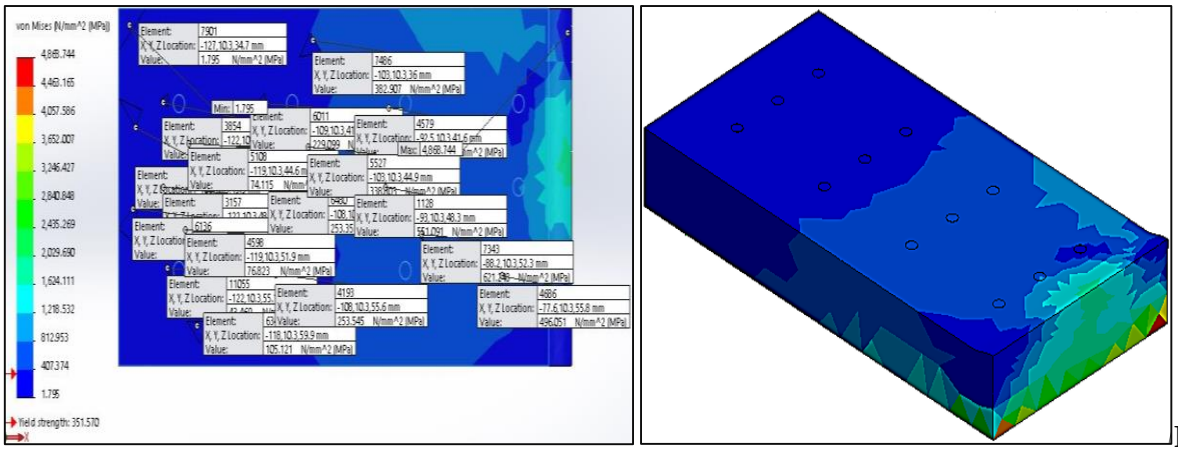

Figure 5. Thermal stress distribution profile at welding temperature of 7350ºF

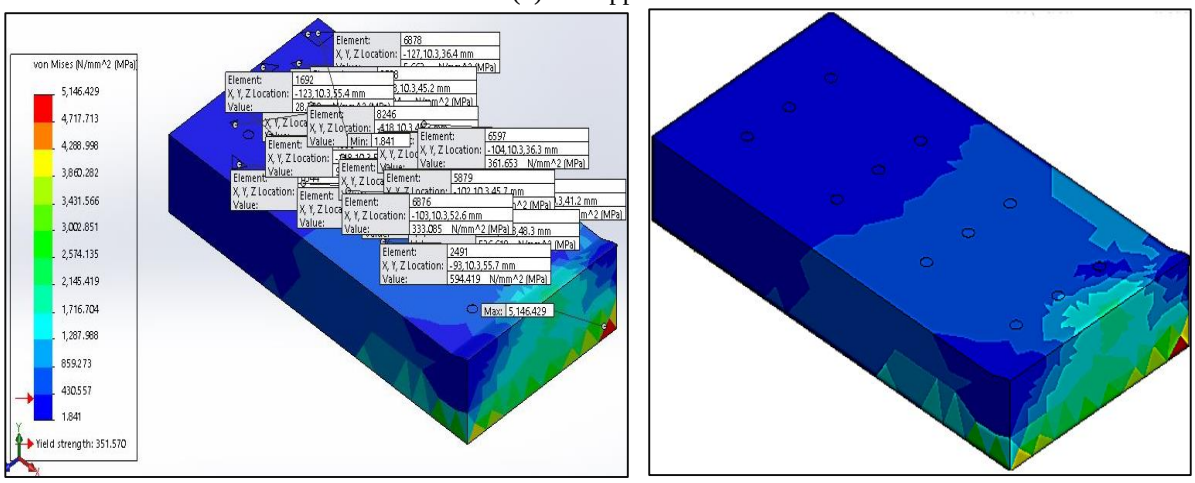

Figure 6. Thermal stress distribution profile at welding temperature of 7600ºF

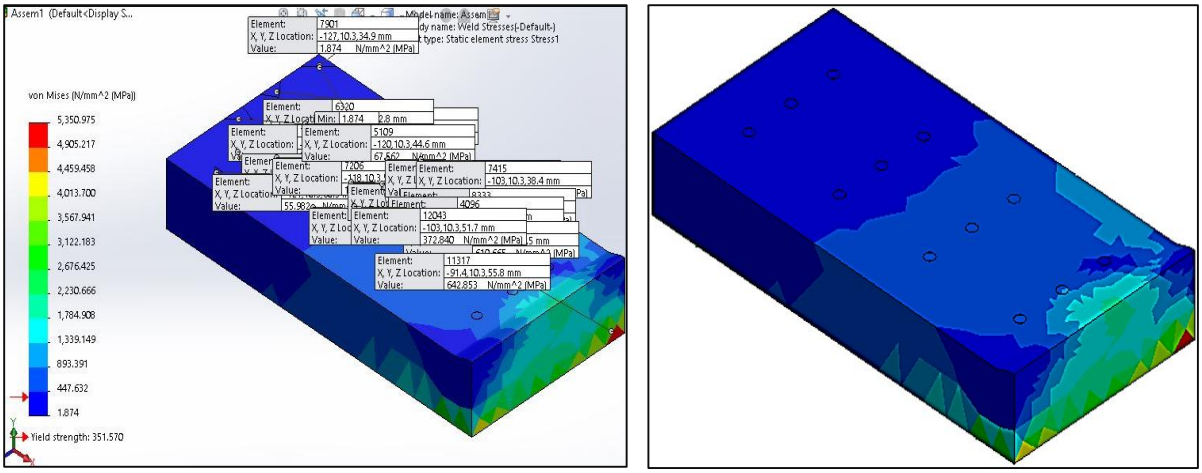

Figure 7. Thermal stress distribution profile at welding temperature of 7820ºF

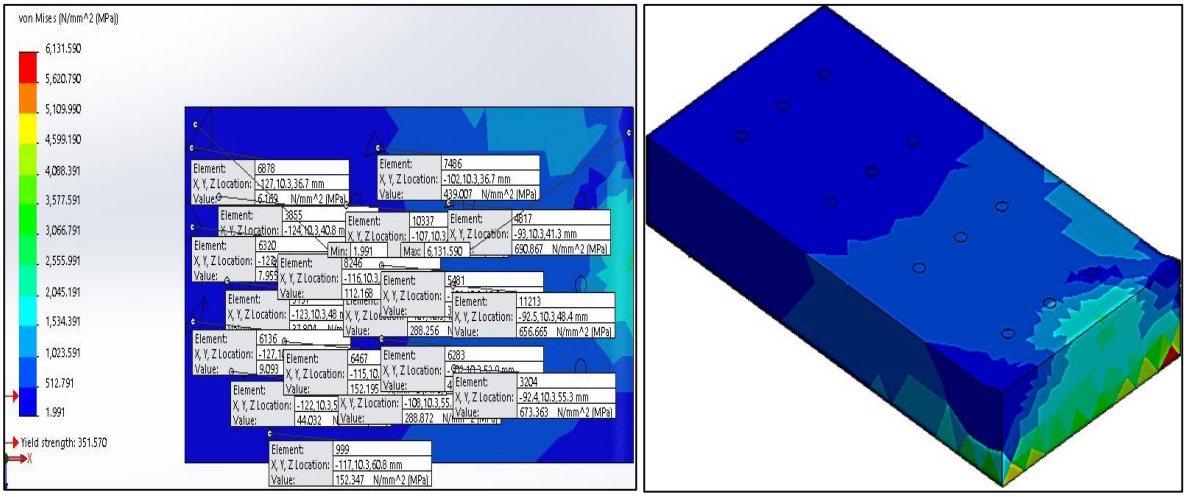

Figure 8. Thermal stress distribution profile at welding temperature of 7960ºF

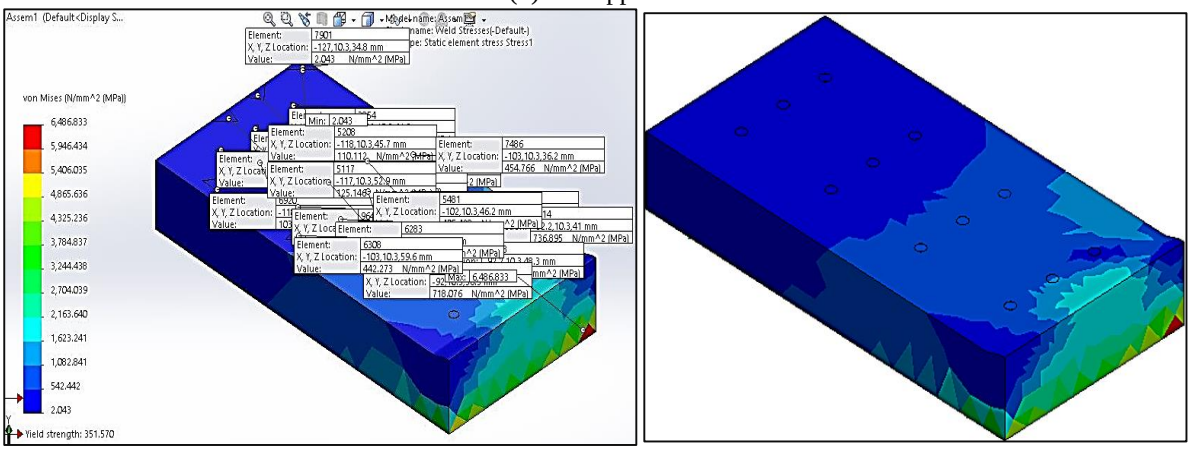

Figure 9. Thermal stress distribution profile at welding temperature of 8000ºF

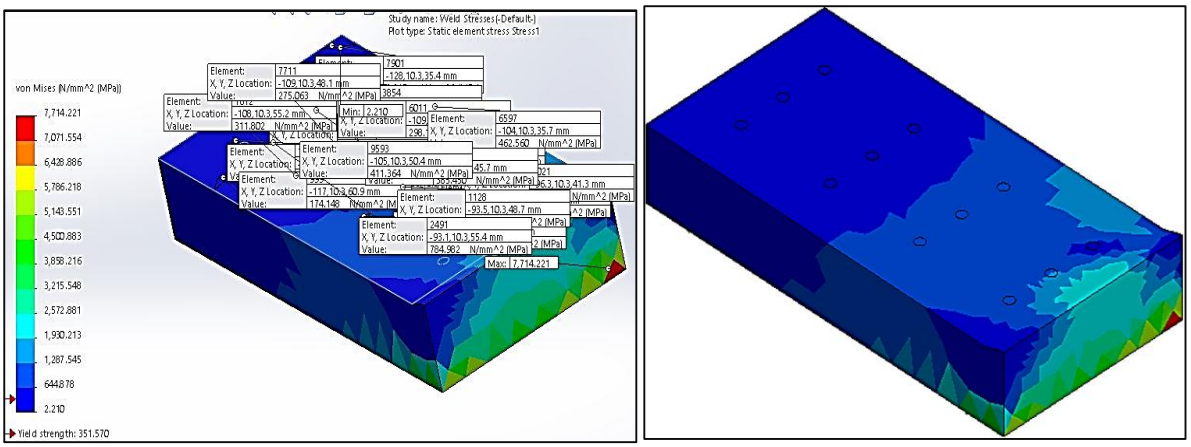

Figure 10. Thermal stress distribution profile at welding temperature of 8180ºF

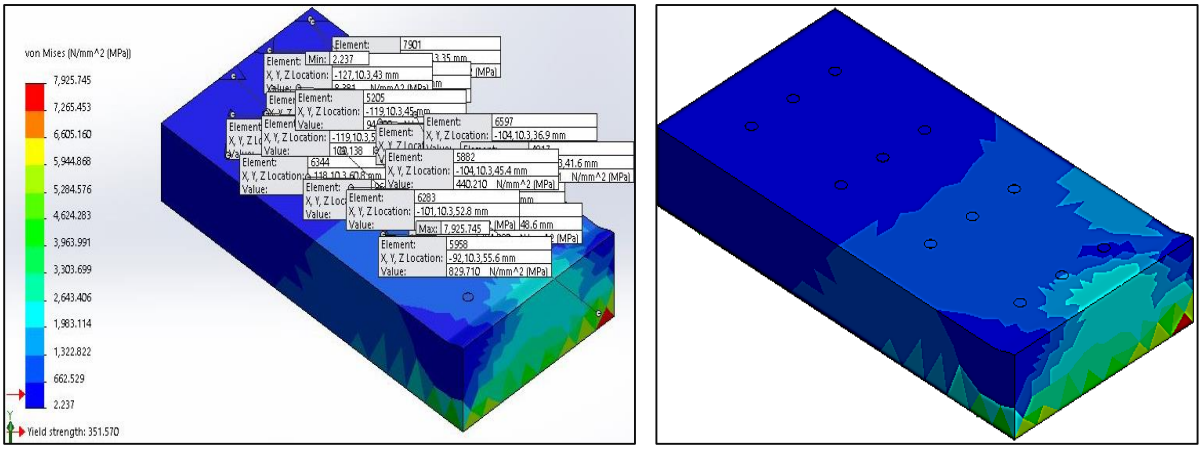

Figure 11. Thermal stress distribution profile at welding temperature of 8400ºF

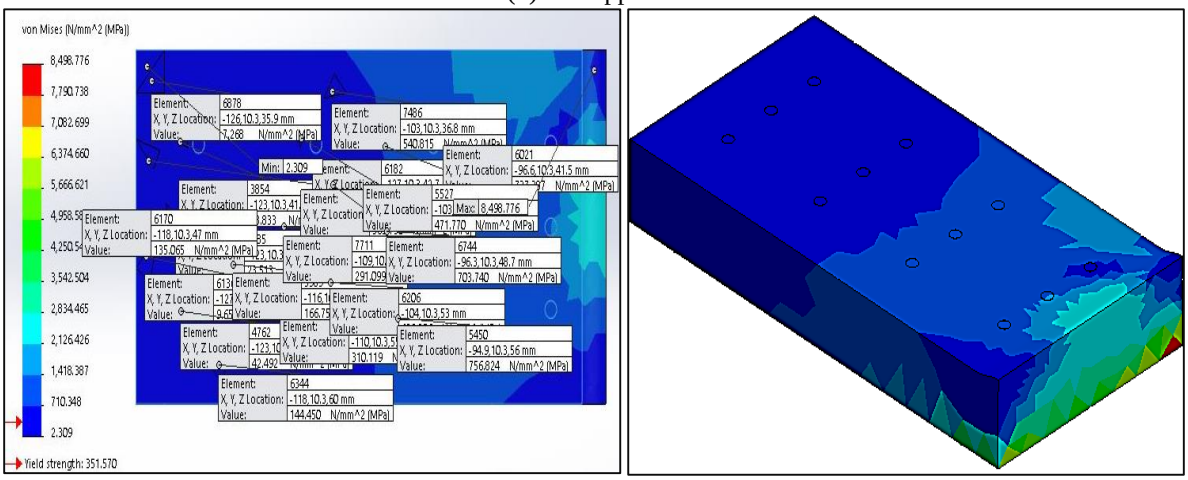

Figure 12. Thermal stress distribution profile at welding temperature of 8620 ºF

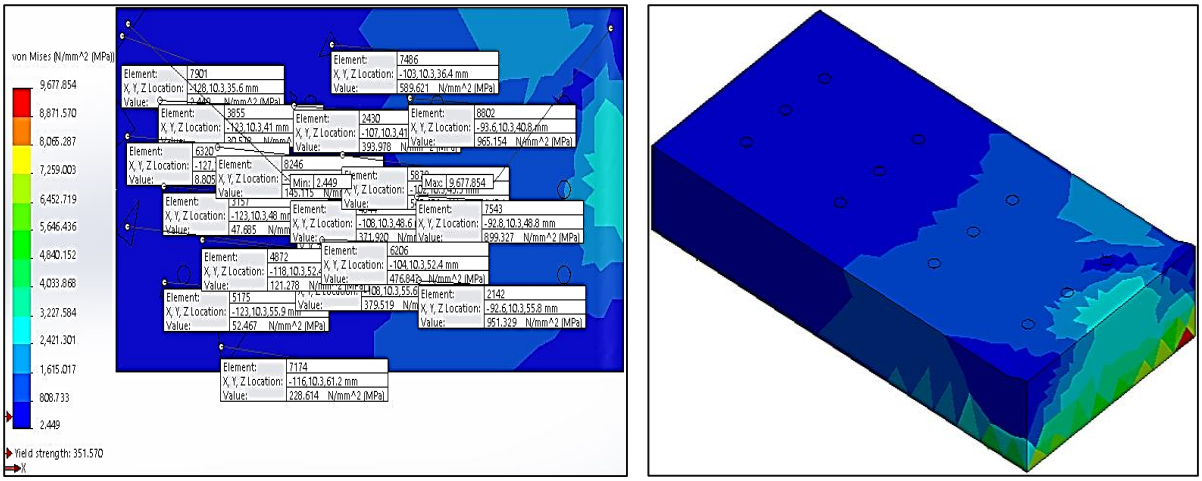

Figure 13. Thermal stress distribution profile at welding temperature of 8876ºF

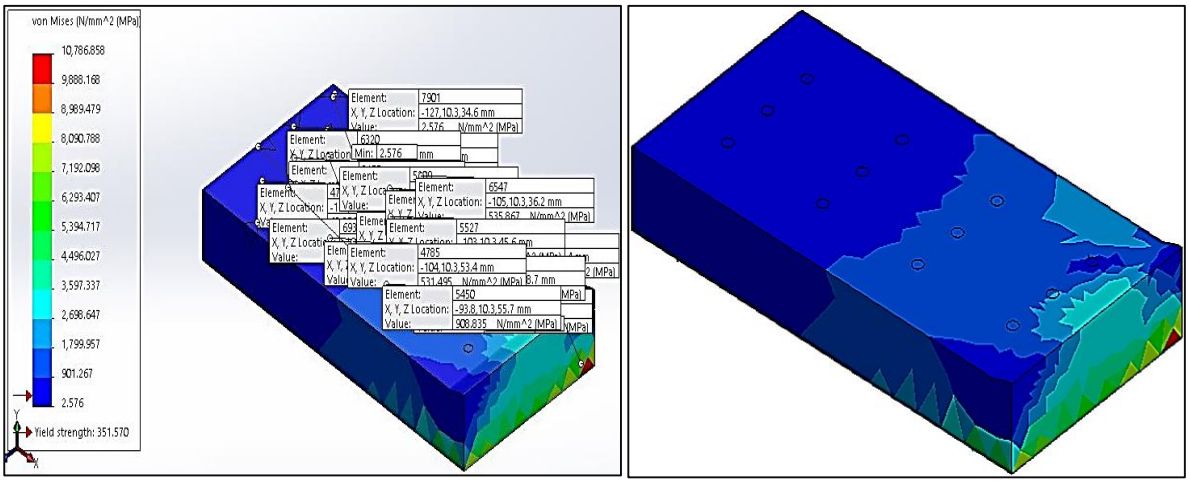

Figure 14. Thermal stress distribution profile at max welding temperature of 9600ºF

Figures 15a-l are extract of Figures 3-14, and are graphical presentations of welding temperature gradient (ºF) with corresponding maximum thermal stress distribution (MPa). Considering the maximum welding temperature (6800, 7100, 7350, 7600, 7820, 7960, 8000, 8180, 8400, 8620, 8876 and 9600ºF) employed in the study, plots of thermal stresses variations experimentally derived from

each of the Twelve (12) welded samples and the aforementioned thermal stress distribution profiles (see Figures 3-14) are graphically presented in Figures 15a-i

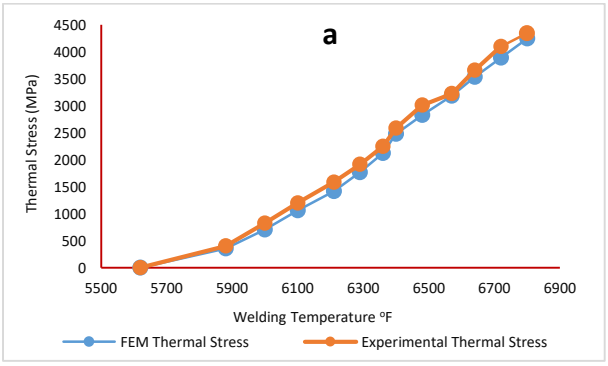

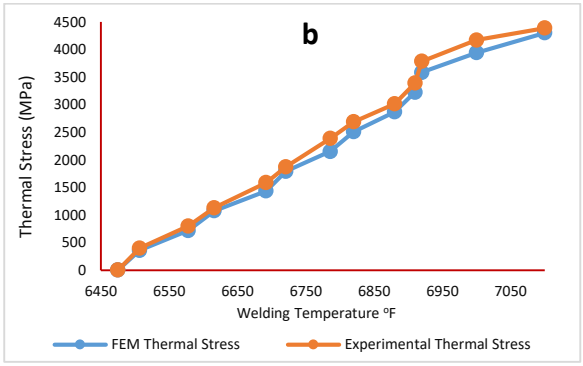

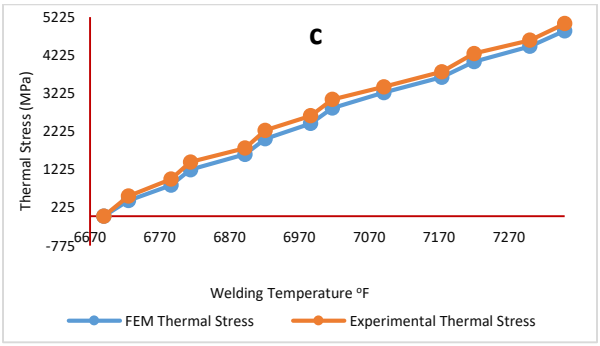

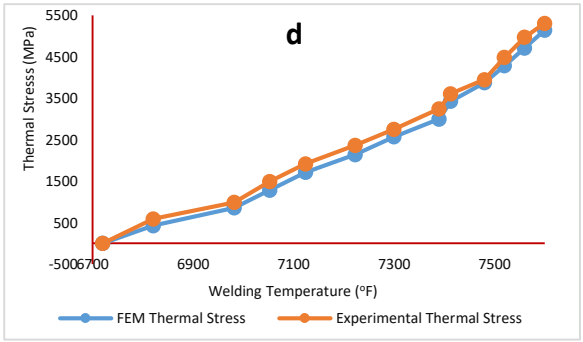

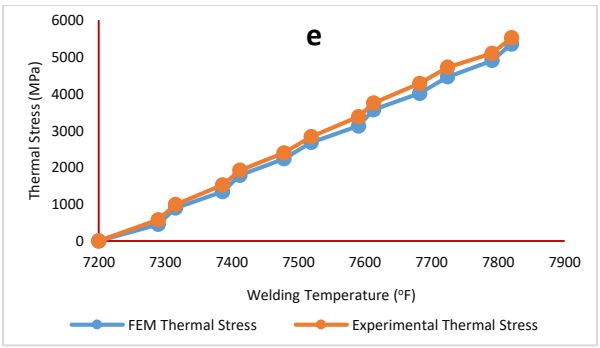

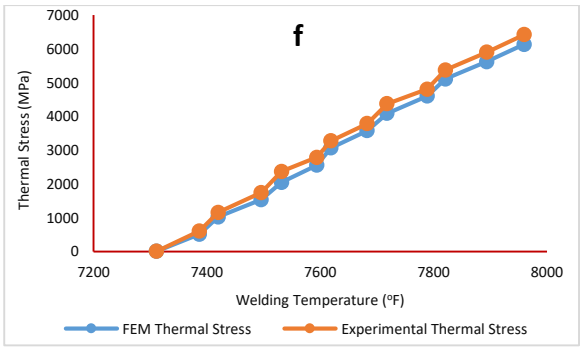

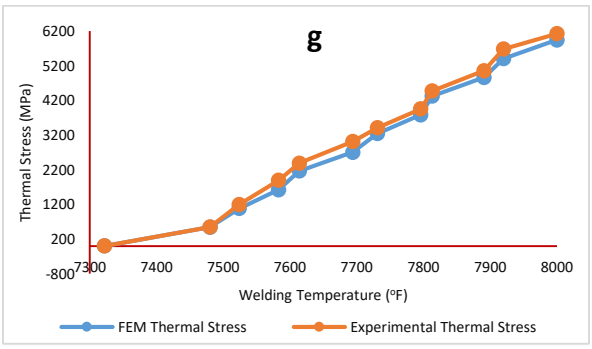

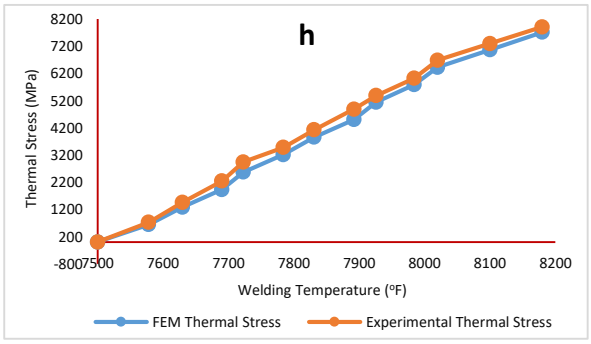

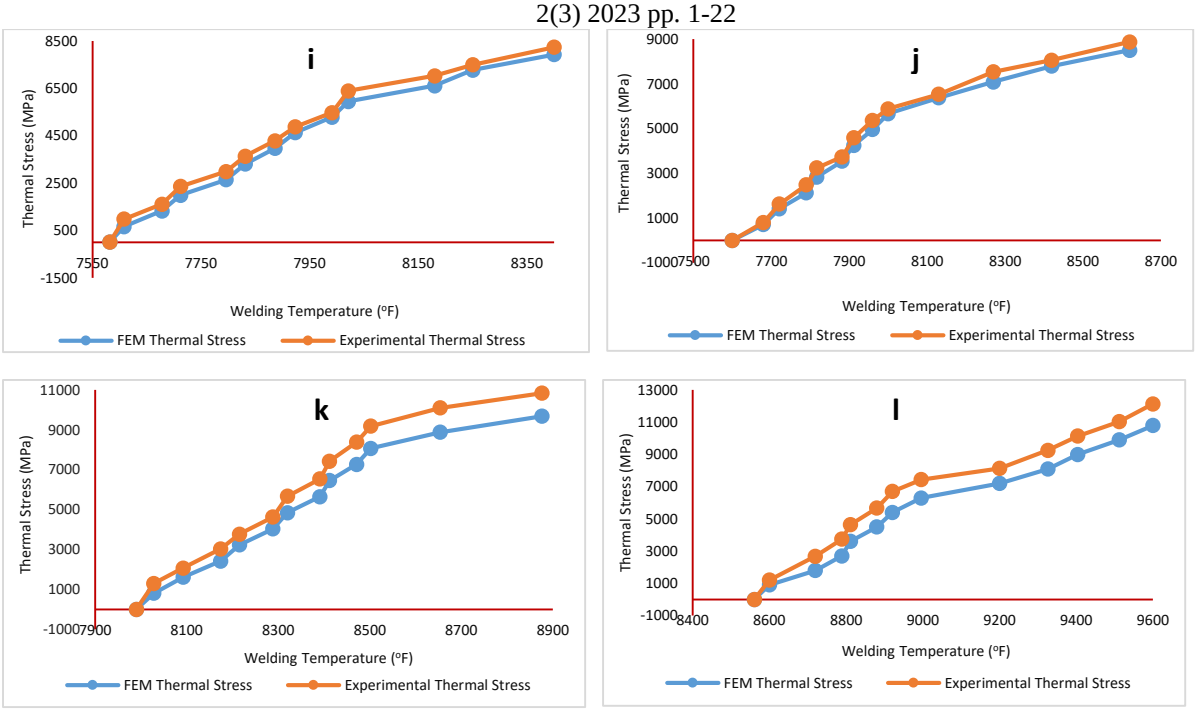

Figure 15a-i. Plots of thermal stress variations against welding temperature

As observed in Figures 15a-l, a significant correlation is established between the FEM-induced thermal stress distribution and the experimentally induced thermal stress distribution. This can be observed in the trend shown on the plots, for example, FEM and Experimentally thermal-induced stresses of 4244.373 and 4345.894 MPa are both observed at a welding temperature of 680^{o}F as graphically illustrated in Figure 15a, while FEM and Experimentally thermal-induced stresses of 10786.858 and 12124.269 MPa are both observed at welding temperature of 9600^{o}F as graphically illustrated in Figure 15l. This implies that Finite Element Method can be adopted as an effective tool in modelling and prediction of thermal stresses induced on welded materials due to variations in welding temperature [47, 48]. All the plots exhibited one common trend depicting the coherent increase in welding temperature and thermal stress which further buttresses the claim stated earlier that welding temperature and thermal stress increase in pari passu as graphically illustrated in Figures 15a-l. It can be observed from the plots (Figures 15a-l) that thermal stress measured at each point of welding temperature varies depending on whether the welding temperature decreases or increases.

4. Conclusıon

The present study modelled and simulated the transient thermal stress behaviour in AISI 1018 flat plates at variable welding temperature regimes, employing FEM and experimental approaches. It was observed that thermally induced stresses are confined within the fusion zone as residual stresses which can expose the material to crack initiation, propagation and fracture which happens to be the final stage of failure, which occurs as a result of progressive crack growth around the regions (plastic regions) where the material can no longer withstand the loads acting on them. Residual stresses induced by the welding process at the time of component manufacturing should be relieved from the material, because, the moment it initiates a crack on the material, the crack propagates rapidly and continues to increase in size. For that reason, post-weld treatment such as mechanical technique (vibratory method or shot peening approaches) and other forms of heat treatment should be employed to mitigate the effect of thermally induced stresses. However, the service life of materials with inherent thermally induced stress can be sustained if the loading conditions which insert

compressive and tensile forces on the material are minimised to an extent where the material yield strength is far from the load capacity and other surrounding forces. Thermally-induced stress values obtained both from the FEM and Experimental TIG welding process revealed that the temperature values graphically sustained a unique pattern and trend. This implied that a remarkable correlation is established between the experimentally induced thermal stress distribution and the FEM-induced thermal stress distribution. Thus, it could be inferred that FEM can be deployed as a veritable tool for modelling and simulation and findings obtained therein sets a framework for future research that emanates from thermal stress distribution to TIG welding.

Nomenclature

Abbreviations

AISI	American Iron and Steel Institute
CCT	Continuous Cooling Transformation
DOE	Design of Experiment DOE
GTAW	Gas Tungsten Arc Welding
FEM	Finite Element Method
EES	Finite Element Solver
FIB-DIC	Focused Ion Beam-Digital Image Correlation
MPa	Mega Pascal
TIG	Tungsten Inert Gas
PWT	Post Weld Treatment
HAZ	Heat Affected Zone
WTSD	Welding Thermal Stress Diagram
3D	3 Dimension

Symbols

t	Time
k	Thermal conductivity
u	Temperature
ΔQ	Change in internal energy per unit volume of the material
C_p	Specific heat capacity
ρ	Mass density of the material
ε_{th}	Thermal strain
α	Coefficient of thermal expansion
α	Total strain across martensite transformation range
ΔT	Temperature variation
x, y, z	Cartesian coordinates
Q	Internal heat
T	Temperature
p	Phase proportion
τ_R	Delay time
n	Exponent related to reaction speed between arc electrode and workpiece
p_m	Phase proportion derived at an infinitely low temperature
M_s and b	Initial transformation temperatures
K	Constant
Δm	Increase in martensite fraction as a function of temperature
f	Martensite fraction as a function of cooling rate
ε^{tr}	Transformation strain
L	Characteristic length of material
T_a	Ambient temperature
Nu	Nusselt number
Pr	Prandtl number
Gr	Grashof number
q_r	Stefan-Boltzmann relation

ε	Heat emissivity
σ	Stephan-Boltzman constant
R	Incompatibility term
P	Pressure of argon shielding gas
μ	Velocity flow of argon shielding gas
^{o}F	Degree Fahrenheit

References

[1] Rong, Y., Xu, J., Huang, Y. and Zhang, G. (2017). Review on finite element analysis of welding deformation and residual stress. Sci. Tech. Wld. Joing. Vol. 23(3), pp.198-208.
[2] Mai, C., Hu, X., Zhang, L., Song, B. and Zheng, X. (2021) Influence of Interlayer Temperature and Welding Sequence on the Temperature, Distribution and Welding Residual Stress of the Saddle-Shaped Joint of Weldolet-Header Butt Welding. Mat. Vol. 14, pp.1-19.
[3] Owunna, I. B. and Ikpe, A. E. (2018). Effects of Parametric Variations on Bead Width of Gas Tungsten Arc Welding of AISI 1020 Low Carbon Steel Plate. Int. J. Eng. Tech. Sci. Vol. 5(3), pp.1-13.
[4] Ghazali, F. A., Manurung, Y. H., Mohamed, M. A., Alias, S. K. and Abdulla, S. (2015). Effect of Process Parameters on the Mechanical Properties and Failure Behavior of Spot Welded Low Carbon Steel. J. Mech. Eng. Sci. Vol. 8, pp.1489-1497.
[5] Yaghi, A. and Becker, A. (2004). State of the Art Review-Weld Simulation Using Finite Element Method. University of Nottingham. UK, Report No: FENET-UNOTT-DLE-08, pp.1-27.
[6] Qian, Z., Chumbley, S. and Johnson, E. (2011). The Effect of Specimen Dimension on Residual Stress Relaxation of Carburized and Quenched Steels. Mat. Sci. Eng. Vol. A529, pp.246-252.
[7] Wei, L., Junjie, M., Fanrong, K., Shuang, L. and Radovan, K. (2015). Numerical Modelling and Experimental Verification of Residual Stress in Autogenous Laser Welding of High-Strength Steel. Lsrs. Manf. Mat. Pros, Vol. 2, pp.24-42.
[8] Law, M., Prask, H., Luzin, V. and Gnaeupel-Harold, T. (2006). Residual Stress Measurements in Coil, Line Pipe and Girth Welded Pipe. Elsevier Science Ltd., Menai.
[9] Owunna, I. B., Ikpe, A. E. and Achebo, J. I. (2018). Temperature and Time Dependent Analysis of Tungsten Inert Gas Welding of Low Carbon Steel Plate using Goldak Model Heat Source. J. App. Sci. Env. Mgt. Vol. 22(11), pp.1719-1725.
[10] Li, C., Chen, Z., Gao, H., Zhang D. and Han, X. (2021). Numerical simulation of the metal inert gas welding process that considers grain heterogeneity. *J. Mat: Des. App.* Vol. 235(1), pp.42-58.
[11] Chen, J., Salvati, E., Uzun, F., Papadaki, C., Wang, Z., Everaerts, J. and Korsunsky, A. (2020). An Experimental and Numerical Analysis of Residual Stresses in A TIG Weldment of Single Crystal Nickel-Based Superalloy. J. Manf. Pros. Vol. 53, pp.190-200.
[12] Withers, P. J., Bhadeshia, H. K. (2001). Residual stress Part 2, Nature and origins. Mat. Sci. Tech. Vol. 17, pp.366-375.
[13] Owunna, I. B. and Ikpe, A. E. (2019). Evaluation of Induced Residual Stresses on AISI 1020 Low Carbon Steel Plate from Experimental and FEM Approach during TIG Welding Process. J. Mech. Eng. Sci. Vol. 13(1), pp.4415-4433.
[14] Mishchenko, A. and Scotti, A. (2021). Welding thermal stress diagrams as a means of assessing material proneness to residual stresses. J. Mat. Sci. Vol. 56, pp.1694-1712.
[15] Owunna, I. B. and Ikpe, A. E. (2019). Finite Element Analysis of Tungsten Inert Gas Welding Temperatures on the Stress Profiles of AIS1 1020 Low Carbon Steel Plate. Int. J. Eng. Tech. Vol. 5(2), pp.50-58, 2019.
[16] Vemanaboina, H., Babu, B. S., Gundabattini, E., Ferro, P. and Kumar, K. (2021). Effect of Heat Input on Distortions and Residual Stresses Induced by Gas Tungsten Arc Welding in SS 316L to INCONEL625 Multipass Dissimilar Welded Joints. *Adv. Mat. Sci. Eng.* Vol. 8, pp.1-9.
[17] Yelamsetti, B. and Rajyalakshmi, G. (2018). Thermal Stress Analysis of Similar and Dissimilar Welded Joints. *UPB Sci. Buln. Sers.* Vol. 80(4), pp.223-240.
[18] Ahmad, A. S., Wu, Y., Gong, H. and Nie, L. (2019). Finite Element Prediction of Residual Stress and Deformation Induced by Double-Pass TIG Welding of Al 2219 Plate. Mat. Vol. 12, pp.1-20.
[19] Owunna, I. B. and Ikpe, A. E. (2021). Experimental and Numerical Optimization of Tungsten Inert Gas (TIG) Welding Process Parameters Relative to Mechanical Properties of AISI 1018 Mild Steel Plate. Adv. Eng. Des. Tech. Vol. 3, pp.132-145.
[20] Ogino, Y., Hirata, Y., Kawata, J. and Nomura, K. (2013). Numerical Analysis of Arc Plasma and Weld Pool Formation by a Tandem TIG Arc. Wld. Wld. Vol. 57, pp.411-423.
[21] Roger, F. and Van, D. K. (2004). Prediction of the weld shape in arc welding A numerical modeling example in Multiphysics coupling. Euro. Fin. Elt. Rev. Vol. 13(5-7), pp.713-724.

[22] Hameed, R. H. and Abed, I. M. (2018). Design Mathematical Model for Heat Transfer in Laser Beam Welding Process. ARPN J. Eng. App. Sci. Vol. 13(21), pp.8372- 8380.
[23] Owunna, I., Ikpe, A. E. and Achebo, J. I. (2018). 3D Finite Element Modelling of Weld Bead Penetration in Tungsten Inert Gas (TIG) Welding of AISI 1020 Low Carbon Steel Plate. Euro. Mech. Sci. Vol. 2(3), pp.96-105.
[24] Mi, G., Li, C., Gao, Z., Zhao, D., and Niu, J. (2014). Finite Element Analysis of Welding Residual Stress of Aluminium Plates under Different Butt Joint Parameters. Eng. Rev. Vol. 34(3), pp.161-166.
[25] Owunna, I. B., Ikpe, A. E. and Ohwoekevwo, J. U. (2022). Application of SEM/EDS in Fractographic investigation of TIG Welded AISI 1020 Fusion Zones at Distinct Welding Current Steps. AridZone J. Eng. Tech. Env. Vol. 18(2), pp.255-266.
[26] Thorat, S. R., Kharde, Y. R., Bhosale, K. C., Kharde, S. B. (2013). Effect of welding conditions on residual stresses and heat source distribution on temperature variations on butt welds: a review. Int. J. Eng. Res. App. Vol. 3(1), pp.1434-1439.
[27] Costa, G. J. and Rio, P. R. (2018). Fundamental aspects of the martensite transformation curve in Fe-Ni-X and Fe-C alloys. J. Mat. Res. Tech. Vol. 7(4), pp.499-507.
[28] Manchón-Gordón, A. F., López-Martín, R., Ipus, J. J., Blázquez, J. S., Svec, P., Sr., Conde, C. F. and Conde, A. (2021). Kinetic Analysis of the Transformation from 14M Martensite to L21 Austenite in Ni-Fe-Ga Melt Spun Ribbons. Met. Vol. 11, pp.1-13.
[29] Celada-Casero, C., Sietsma, J. and Santofimia, M. J. (2019). The role of the austenite grain size in the martensitic transformation in low carbon steels. Mat Des. Vol. 167, pp.1-10.
[30] Dai, Q. X., Cheng, X. N., Zhao, Y. T., Luo, X. M. and Yuan, Z. Z. (2004). Design of martensite transformation temperature by calculation for austenitic steels. Mat. Charn. Vol. 52, pp.349-354.
[31] Mirhosseini, S., Perdahcıoğlu, E. S., Atzema, E. H. and Boogaard, A. H. (2022). Effect of temperature and heat generation on martensitic phase transformation in DH steels. Mat, Vol. 14, pp.1-9.
[32] Radaj, D. (2012). Heat Effects of Welding: Temperature Field, Residual Stress, Distortion. Springer Berlin, Heidelberg, ISBN: 978-3-642-48640-1.
[33] Owunna, I. and Ikpe, A. E. (2019). Modelling and Prediction of the Mechanical Properties of TIG Welded Joint for AISI 4130 Low Carbon Steel Plates Using Artificial Neural Network (ANN) Approach. Nig. J. Tech. Vol. 38(1), pp.117-126.
[34] Gery, D., Long, H. and Maropoulos, P. (2005). Effects of welding speed, energy input and heat source distribution on temperature variations in butt joint welding. J. Mat. Pros. Tech. Vol. 167, pp.393-401.
[35] Chen, J., Salvati, E., Uzun, F., Papadaki, C., Wang, Z., Everaerts, J. and Korsunsky, A. M. (2020). An experimental and numerical analysis of residual stresses in a TIG weldment of a single crystal nickel-base superalloy. J. Manf. Pros. Vol. 53, pp.190-200.
[36] Liu, Y., Wang, P., Fang, H. and Ma, N. (2021). Mitigation of residual stress and deformation induced by TIG welding in thin-walled pipes through external constraint. J. Mat. Res. Tech. Vol. 15, pp.4636-4651.
[37] Turski, M., Francis, J. A., Hurrenl, P. R., Bate, S. K., Hiller, S. and Withers, P. J. (2012). Effects of stopstart features on residual stresses in a multi-pass austenitic stainless steel weld. Int. J. Pres. Ves. Pip. Vol. 89, pp.9-18.
[38] Liang, W., Murakawa, H. and Deng, D. (2015). Investigation of welding residual stress distribution in a thick-plate joint with an emphasis on the features near weld end-start. Mat. Des. Vol. 67, pp.303-312.
[39] Zurlo, G. and Truskinovsky, L. (2018). Inelastic surface growth. Mech. Res. Com. Vol. 93, pp.174-179.
[40] Zaza, D., Ciavarella, M. and Zurlo, G. (2021). Strain incompatibility as a source of residual stress in welding and additive manufacturing. Euro. J. Mech. Vol. 85, pp.104-147.
[41] Rao, Z. H., Hu, J., Liao, S. M. and Tsai, H. L. (2009). Study the Shielding Gas Effect on the Metal Transfer and Weld Pool Dynamics in GMAW. Proceedings of HT2009 2009 ASME Summer Heat Transfer Conference July 19-23, 2009, San Francisco, California USA.
[42] Yelamsetti, B. and Rajyalakshmi, G. (2018). Thermal Stress Analysis of Similar and Dissimilar Welded Joints. UPB Sci. Bttn. Ser. Vol. 80(4), pp.223-240.
[43] Zhang, H., Ouyang, Z., Li, L., Ma, W., Liu, Y., Chen, F. and Xiao, X. (2022). Numerical Study on Welding Residual Stress Distribution of Corrugated Steel Webs. Met. Vol. 12(1831), pp. 1-20.
[44] Paradowska, A. M. and Zhao, Z. (2010). Stress Relieving and its Effect on Life of Welded Tubular Joints. Eng. Flr. Ana. Vol. 17(1), 320-327.
[45] Kang, H. T., Lee, Y. and Sun, X. J. (2008) Effects of Residual Stress and Heat Treatments on Fatigue Strength of Weldments. Mat. Sci. Eng: A. Vol. 497(1-2), pp.37-43.
[46] Hatamleh, O., Rivero, I. and Lyons, J. (2007). Evaluation of surface residual stresses in friction stir welds due to laser and shot peening. J. Mat. Eng. Perf. Vol. 16, pp.549-553.
[47] Chidiac, S. E. and Mirza, F. A. (1993). Thermal Stress Analysis Due to Welding Processes by the Finite Element Method. Com. Strut. Vol. 46(3), pp.407-412.
[48] Gedney, B. L. and Rizos, D. C. (2022). Combining welding-induced residual stress with thermal and mechanical stress in continuous welded rail. Rst. Eng. Vol. 16, pp.1-16.